Intrinsic Dual-Energy Processing of Myocardial Perfusion Images

J. Keenan Brown, H. Roger Tang, Robert S. Hattner, Moshe Bocher, Neil W. Ratzlaff, Prajoy P. Kadkade, Bruce H. Hasegawa, and Elias H. Botvinick

Physics Research Laboratory, University of California, San Francisco, South San Francisco; and Joint Bioengineering Graduate Group; Nuclear Medicine Section, Cardiovascular Division; and Cardiovascular Research Institute, University of California, San Francisco, San Francisco, California

We have developed a software-based method for processing dual-energy ^{201}Tl SPECT emission projection data with the goal of calculating a spatially dependent index of the local impact of γ-ray attenuation. We refer to this method as intrinsic dual-energy processing (IDEP). **Methods:** IDEP exploits the differential attenuation of lower energy emissions (69–83 keV) and higher energy emissions (167 keV) resulting from the decay of ^{201}Tl to characterize the relative degree of low-energy γ-ray attenuation throughout the myocardium. In particular, IDEP can be used to estimate the relative probability that a low-energy γ-ray emitted from a particular region of the myocardium is detected during the acquisition of SPECT projection data. Studies on phantoms and healthy human volunteers were performed to determine whether the IDEP method yielded detection probability images with systematic structure visible above the noise of these images and whether the systematic structure in the detection probability images could be rationalized physically. In patient studies, the relative regional detection probabilities were applied qualitatively to determine the likely effects of attenuation on the distribution of mapped photon emissions. **Results:** Measurements of the detection probability in uniform phantoms showed excellent agreement with those obtained from computer simulations for both 180° and 360° acquisitions. Additional simulations with digital phantoms showed good correlation between IDEP-estimated detection probabilities and calculated detection probabilities. In patient studies, the IDEP-derived detection probability maps showed qualitative agreement with known nonuniform attenuation characteristics of the human thorax. When IDEP data were integrated with the findings on the emission scan, the correlation with coronary anatomy (known in 6 patients and hypothesized on the basis of clinical and electrocardiographic parameters in 5 patients) was improved compared with evaluating the mapped emission image alone. **Conclusion:** The IDEP method has the potential to characterize the attenuation properties of an object without use of a separate transmission scan. Coupled with the emission data, it may aid coronary diagnosis.

Key Words: attenuation correction; myocardial perfusion; SPECT; ^{201}Tl

J Nucl Med 2000; 41:1287–1297

Received May 10, 1999; revision accepted Oct. 27, 1999.

For correspondence or reprints contact: Elias H. Botvinick, MD, Nuclear Medicine Section, Box 0252, L340, University of California, San Francisco, San Francisco, CA 94143.

SPECT myocardial perfusion imaging (MPI) has significant prognostic value and sensitivity in the range of 85%–95%. However, the specificity of SPECT has been commonly reported to be as low as 60%–80%, indicating 20%–40% false-positive readings in some studies (*1–3*). Among several physical factors that degrade image quality and quantitative accuracy in SPECT, photon attenuation is believed to be the major cause of false-positive cardiac SPECT perfusion images (*4–7*). Clinical manifestations of attenuation include false-positive readings in the anterior region of the heart when breast attenuation is significant and false-positive inferior wall readings from significant diaphragmatic attenuation. Sensitivity also may be adversely affected by attenuation-related reductions in apparent regional uptake, which can mask true perfusion defects. These observations have spawned extensive research into methods to compensate for photon attenuation in SPECT images.

Sufficient progress has been made in terms of instrumentation, computational power, and software design so that today, most SPECT manufacturers have developed systems to perform compensation for photon attenuation. These methods require reconstruction of a patient-specific attenuation map from transmission data acquired using an external radiation source and the scintillation camera (*8–11*). The patient-specific attenuation map then is incorporated into an iterative reconstruction algorithm to correct the SPECT data for photon attenuation (*12–15*).

In comparison with the direct or extrinsic methods for handling attenuation compensation, intrinsic methods that do not require a transmission measurement to generate an attenuation map have also been proposed (*16–23*). In principle, these methods could be rapidly implemented at all SPECT centers without substantial expense to purchase, operate, and maintain hardware for performing transmission imaging on a SPECT system.

Hansen and Siegel (*22*) evaluated a method to attenuation compensate cardiac ^{201}Tl SPECT images using a technique that requires neither a transmission scan nor an additional emission image or additional radiopharmaceutical. Rather, they exploited the differential attenuation of low-energy photons emitted by ^{201}Tl (mercury x-rays in the range of

69–83 keV) compared with high-energy γ-rays emitted by ^{201}Tl (167 keV). Because the high- and low-energy photons are emitted with identical spatial distributions, and because the high-energy γ-rays undergo less attenuation than the low-energy emissions, measurements of the number of photons detected in high- and low-energy windows intrinsically provide information about the amount of attenuator between the points of emission and the points of detection. Hansen and Siegel used a simple point-source model to estimate a factor to correct the low-energy emission data for the effects of attenuation. Although imperfect (*24*), the correction factor model used by Hansen and Siegel showed qualitative improvements consistent with expectations in limited phantom and patient studies. In particular, corrected images showed a greater increase in activity near the base of the heart than near the apex. However, the corrected images also exhibited noise degradation, presumably associated with the relatively small number of counts in the high-energy window relative to the low-energy window, that contributes to noise in the derived correction factor.

Instead of attempting to correct ^{201}Tl SPECT images for the effects of attenuation, in this study we describe a method of characterizing the effects of attenuation. We report the theory and preliminary applications of a new software-based method for processing dual-energy ^{201}Tl SPECT emission projection data with the goal of calculating a spatially dependent index of the local impact of γ-ray attenuation.

MATERIALS AND METHODS

Conceptual Description of Intrinsic Dual-Energy Processing

We have developed an intrinsic technique for assessing MPI using dual-energy emission projection data from ^{201}Tl perfusion scans. We refer to this method as intrinsic dual-energy processing (IDEP). Similar to the method of Hansen and Siegel (*22*), IDEP uses the differential attenuation of high- and low-energy photons emitted by ^{201}Tl to characterize nonuniform attenuation within the thorax. However, an important and critical distinction between IDEP and the method of Hansen and Siegel is that IDEP explicitly includes information regarding the distribution of radionuclide within the patient and does not rely on the point-source approximation used by Hansen and Siegel. Rather, IDEP uses a reconstructed emission image of the myocardium as an initial estimate of the radionuclide source distribution.

In addition, IDEP calculates a detection probability map that, on a pixel-by-pixel basis, gives the relative probability that a primary photon emitted within a particular region is detected by the SPECT system. The pixel values in the detection probability map provide an index of attenuation on a pixel-by-pixel basis, in which lower detection probabilities are associated with regions where emission photons suffer a greater degree of attenuation and higher detection probabilities are associated with regions where attenuation is of less concern. For example, emissions within regions of the myocardium that undergo significant breast or diaphragmatic attenuation will have a lower detection probability than that calculated for other regions within the myocardium. Conversely, apparent deficits in tracer uptake in regions with relatively high detection probabilities are more likely to provide accurate measures of myocardial status. The absolute value of this probability also depends on other factors, including quantum efficiency of the detector and the type of collimator used on the camera. However, these factors uniformly alter the detection efficiency (i.e., detection probability) throughout the camera field of view. Therefore, they are essentially normalized in the detection probability map and have little influence on its interpretation.

Theory

IDEP starts by assuming that the radionuclide distribution within the object can be estimated using filtered backprojection (FBP) or another reconstruction technique. The reconstructed radionuclide distribution then is considered to be placed so that it overlaps with a semi-infinite, uniformly attenuating region that has a normal axis that coincides with that of the scintillation camera. As indicated in Figure 1, a detector is positioned at the point represented by each pixel in the emission projection data. Given this geometry, the

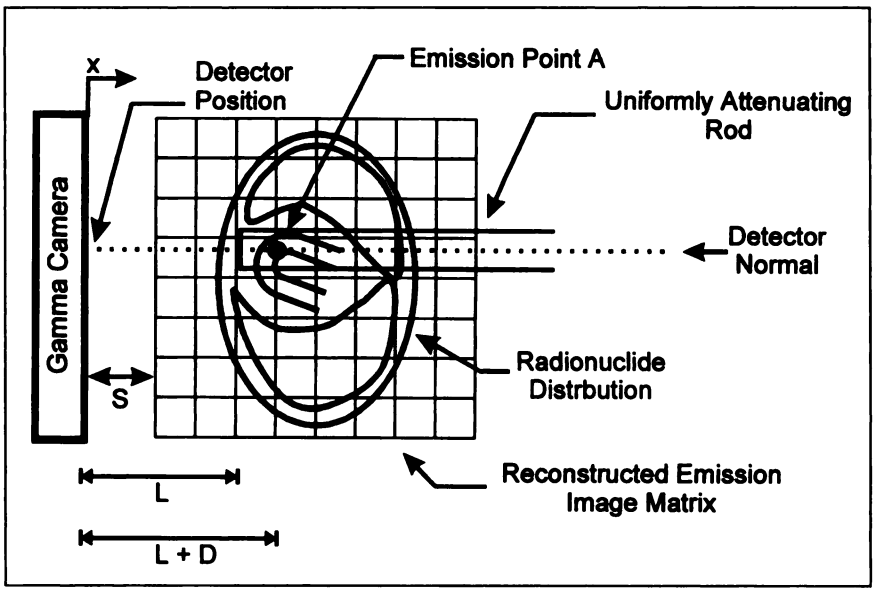

FIGURE 1. Schematic diagram illustrating IDEP technique. For illustrated detection position, γ-rays emitted from point A must traverse length D of attenuating material and therefore are detected with relative detection probability of $\eta = \exp(-\mu D)$. S = distance to edge of bitmap; L = distance to front face of attenuating region.

objective of IDEP is to find the position of the attenuating region, measured as the distance L between the front surface of the attenuating region and the position of the detector, such that the ratio of the number of high- and low-energy emission photons counted at the particular detection point is consistent with what would be detected for the radionuclide distribution estimated from FBP and the position of the attenuating region. The resulting geometric information is used to calculate detection probabilities to characterize the effects of attenuation on the detected emission data.

Mathematically, we assume that the radionuclide concentration $\rho(x)$ is a function of position x along a detector normal (Fig. 1) and that $x = 0$ is located at the detector. Also, we assume $\rho(x) = 0$ for positions x outside the radionuclide distribution bitmap and that the near edge of the radionuclide bitmap is a distance S from the detector (Fig. 1). The objective of the calculation is to find the distance, L, from the detector to the front face of the attenuating region such that

$$\left[\frac{N^{high}}{N^{low}}\right] = \left[\frac{N_o^{high}}{N_o^{low}}\right] \frac{\int_S^L \rho(x)dx + \int_L^\infty \exp[-\mu_{high}(x - L)]\rho(x)dx}{\int_S^L \rho(x)dx + \int_L^\infty \exp[-\mu_{low}(x - L)]\rho(x)dx}, \quad \text{Eq. 1}$$

where N_o^{high} (N_o^{low}) is the number of high-energy (low-energy) photons emitted per unit measurement time with an ideal detector; N^{high} and N^{low} represent the number of high- and low-energy photons, respectively, detected from the ^{201}Tl distribution imaged by the scintillation camera and recorded at a given pixel of the emission projection data; and μ_{low} and μ_{high} are the linear attenuation coefficients for the low-energy and high-energy radionuclide photons for the modeled water-equivalent attenuating region. Conceptually, the first integral in the numerator and denominator of Equation 1 is proportional to the expected number of detected counts attributed to radionuclide in the unattenuated region between the detector and the face of the modeled attenuating region, whereas the second integral is proportional to the expected number of counts from radionuclide within the uniformly attenuating region. The relevant proportionality constants are N_o^{high} for the numerator (high-energy window) and N_o^{low} for the denominator (low-energy window).

To efficiently determine L in Equation 1, given the number of detected counts in the high- and low-energy windows for a given emission detection point, we note that the first integral in the numerator and denominator of Equation 1 is small relative to the second integrals for emission positions where a significant number of emission photons were detected (e.g., for projections viewing the myocardium). In this case, it can be shown that

$$\left[\frac{N^{high}}{N^{low}}\right] = \left[\frac{N_o^{high}}{N_o^{low}}\right] \frac{\exp[\mu_{high}(L - S)] \int_S^\infty \exp[-\mu_{high}(x - S)]\rho(x)dx}{\exp[\mu_{low}(L - S)] \int_S^\infty \exp[-\mu_{low}(x - S)]\rho(x)dx}. \quad \text{Eq. 2}$$

The important aspect of Equation 2 is that the integrals no longer carry L dependence, and so Equation 2 can be inverted to give an explicit expression for L in terms of the measured quantities N^{high} and N^{low}. We note the line integrals that appear in Equation 2 are attenuated line integrals that can be easily calculated using ray-tracing techniques (*25*).

Given the position of the attenuating region relative to the detector, calculated as described above, we can estimate the relative probability that a γ-ray emitted from a particular position within the attenuating region is detected by the detector. For example, consider the emission point labeled A in Figure 1. For the detector position illustrated in Figure 1, assume that the leading surface of the attenuating region is located at a distance L from the detector, and emission point A is a distance D inside the attenuating region. We also assume that emissions occurring between the attenuating regions and the detector are detected with a relative probability of 1. Thus, the relative detection probability at emission point A for this particular projection is

$$\eta = \exp(-\mu D), \quad \text{Eq. 3}$$

where μ is the attenuation coefficient of the attenuating region at the energy of the emitted photon. This calculation is repeated for emission point A by deriving the position L of the attenuating region for each detector bin that views a particular emission point. The pixel value in the probability map then is calculated as the arithmetic mean of the relative detection probabilities for each emission point for each detector that views it.

Parameter Estimation

It is apparent that 3 parameters are needed to perform the calculations described: the high-energy, γ-ray attenuation coefficient μ_{high}; the low-energy, γ-ray attenuation coefficient μ_{low}; and the ratio of high- and low-energy primary photons N_o^{high}/N_o^{low} emitted by the radionuclide. Although these parameters appear to be independent physical parameters, they also depend on the measurement technique and other external factors. For example, the ratio of the number of high-energy (167 keV) and low-energy (69- to 83-keV Hg x-rays) photons for ^{201}Tl is known to be very nearly 1:10. However, the experimentally measured value of this ratio with a particular detector (scintillation camera) depends on factors such as the quantum efficiency of the detector at the high and low energies and the choice of energy windows for the measurement. Similarly, because of scatter, an apparent linear attenuation coefficient can be somewhat smaller than the true linear attenuation coefficient.

Therefore, we have performed various calculations to estimate values for these parameters. All calculations used for determining parameters are based on a simple cylindric phantom with a diameter of 20 cm. The phantom was assumed to be a homogeneous volume containing an aqueous solution of ^{201}Tl. The model incorporated a detector capable of discriminating detected events into 1 of 3 energy windows: a low-energy window from 67.5 to 82.5 keV, a high-energy window from 153 to 187 keV, and an implicit window for all other detected counts (which were ignored). The model assumed an energy resolution for the detector of 16.9 keV (full width at half maximum [FWHM]) at 170 keV and 9 keV (FWHM) at 75 keV. These parameters are consistent with the performance and settings on the scintillation cameras used for these preliminary studies (600XR/T; General Electric Medical Systems, Milwaukee, WI; and Orbiter; Siemens Medical Systems, Hoffman Estates, IL). The model accounted for the emission and detection of ^{201}Tl γ-rays with primary energies within the low- and high-energy windows defined above. Within this model, a γ-ray was assumed to be detected either without scattering or after a single Compton scatter. Thus, all higher order scatter events were ignored. In addition, the Compton differential scattering cross section was assumed to be isotropic, which affects only the calculation of the

parameters near the boundary of the cylinder. These simplifying assumptions result in a set of model equations that can be numerically integrated. The validity of these assumptions was checked against a Monte Carlo simulation (including elastic, Compton, and photoelectric scattering) for this geometry using the EGS4 Monte Carlo package (*26*). No significant deviations in the IDEP parameter estimates were observed for the cases investigated with the approximate numeric and the Monte Carlo simulations. The benefit of this approximate approach is that it is easy to investigate the impact of various parameters, such as energy window settings or camera resolution. What was ultimately extracted from these simulations were estimates for the 3 parameters outlined above (i.e., μ_{high}, μ_{low}, and N_0^{high}/N_0^{low}).

We realize that, in practice, detected scattered photons in the lower energy photopeak window have an effect on the specific values of the parameters used to calculate the detection probability. This problem may need to be dealt with in further refinements of the IDEP approach. Here, we simply confirm our Monte Carlo calculations using an experimental phantom measurement.

Uniformity Phantom

The numeric method for determining IDEP parameters was checked experimentally by imaging a 20-cm-diameter acrylic cylindric phantom filled with an aqueous solution containing 7.4 MBq (200 μCi) ^{201}Tl. The phantom was imaged with a 600XR/T scintillation camera using a low-energy, high-resolution collimator and high- and low-energy windows from 153 to 187 keV (20% width centered at 170 keV) and from 67.5 to 82.5 keV (20% width centered at 75 keV), respectively. Two sets of dual-energy emission projection data were collected. The first dataset was acquired with 32 views over 180° at 30 s per view. The second dataset was acquired with 64 views over 360° at 60 s per view. A zoom factor of 2 was used, giving an emission pixel size of approximately 4.32 mm. The emission projection data then were transferred to a computer workstation for processing (conventional as well as dual energy).

The low-energy-window projection data were reconstructed as 64 × 64 arrays using a conventional FBP reconstruction code with a Butterworth filter (0.45 cutoff, eighth order). The resulting images provided the radionuclide distribution estimate needed in the calculation of detection probabilities with IDEP using the parameter values determined from simulation as described. The accuracy of the resulting detection probability images was characterized by comparing profiles through the center of the cylinder in the detection probability images obtained from the phantom study with those predicted using computer simulation (including primary and single-scattered Compton photons).

Computer Simulations

Simulated acquisition and processing of a digital anthropomorphic phantom (the 3-dimensional mathematic cardiac torso, or MCAT, phantom developed at the University of North Carolina at Chapel Hill (*27*)) were performed to assess the correlation between IDEP-calculated detection probabilities and the probability of detection calculated from the known attenuation image. The MCAT phantom, although imperfect, provides a convenient, well-recognized standard from which we can numerically compare the estimate of the detection probability using IDEP with that calculated directly from the attenuation distribution. We are well aware that the digital phantom is not necessarily representative of all or any of the possible clinical anatomies that may exist.

First, we created digital bitmaps that simulate the distribution of ^{201}Tl in the anatomies of a large woman and a normal-sized man with relative activity concentrations of 430, 193, 63, and 20 in the heart, liver, lung, and background, respectively. Next, 2 different attenuation maps for the phantoms, 1 appropriate for the low-energy photon emissions of ^{201}Tl and 1 appropriate for the high-energy photon emissions, were created assuming the linear attenuation coefficients listed in Table 1. Projection data were generated from the digital phantoms to simulate a typical 180° right anterior oblique–left posterior oblique (RAO–LPO) cardiac acquisition using a low-energy, high-resolution collimator. Projection data were calculated for both the low-energy photons and the high-energy photons using the appropriate attenuation maps and assuming a low-to-high detection ratio of 9.1:1 (determined through the parameter estimation calculations as described).

After first reconstructing the projected data using FBP (Butterworth filter of order 8 and 0.45 cutoff), the resulting counts from the low-energy and high-energy windows were used to estimate the detection probability image using IDEP assuming a relative low-to-high attenuation value of 5:4 (estimated from parameter estimation as described) and a 9.1:1 low-to-high photon detection ratio. For comparison, the detection probability maps were also calculated by performing line integrals through the low-energy attenuation maps using ray-tracing techniques (*25*).

The reconstructed emission images of the heart were reoriented into short-axis slices, and the maximum pixel values along radial lines from the center of the heart were plotted onto a polar map, with the center of the polar map representing the apex of the heart. The corresponding pixels in the IDEP-estimated detection probability images and attenuation map-calculated detection probability images were obtained by recording the value of the detection probability at each (maximum) emission pixel used in constructing the emission polar plots.

Patient Studies

Preliminary patient studies were conducted to test the clinical potential of IDEP and the use of detection probabilities as a method for assessing the impact of attenuation on stress myocardial perfusion images. The primary goals of these initial studies were to determine whether the IDEP method yielded detection probability images with systematic structure visible above the noise in these images and to determine whether the systematic structure in the detection probability images could be rationalized physically. For the purposes of this study, 11 patients (7 studied with dipyridamole and 4 studied with exercise stress) were evaluated with the ^{201}Tl stress/4-h redistribution protocol. This protocol was applied to image all patients presenting randomly for stress perfusion imaging on 1 d during each of 3 consecutive weeks. Each patient was imaged using a standard ^{201}Tl stress/^{201}Tl redistribution protocol with dual-energy acquisition using an Orbiter scintillation camera. The SPECT projection data were acquired at 32 views over 180° (RAO–LPO), onto a 64 × 64 matrix, with 20 s per view using a

TABLE 1
Linear Attenuation Coefficients for MCAT Simulation Study

Material	Linear attenuation coefficient (1/cm)	
	75 keV	170 keV
Soft tissue	0.15	0.12
Lung	0.05	0.04
Bone (ribs and spine)	0.18	0.144

low-energy, general-purpose collimator. The energy windows matched those used for the simulations and phantom studies (i.e., 20% energy windows centered at 75 and 170 keV). The stress emission projection data were transferred to a MicroDelta computer (Siemens) for conventional clinical processing and to a separate computer workstation for IDEP processing. In each case, the emission projection data from the low-energy window were reconstructed using a conventional FBP code with a Butterworth filter (0.45 cutoff, eighth order). The resulting emission tomograms were used as estimated radionuclide distributions, and average (relative) detection probabilities were calculated from the dual-energy projection data as described. The processed stress image data—including short-axis and long-axis emission slices, emission polar plots, emission–detection probability overlays, and detection probability polar plots—were reformatted, and hard copies were generated. In each case, defects in the anterior, anterior septum, and apical left ventricular walls were related to left anterior descending coronary artery stenosis; defects in the inferior wall or posterior septum were related to right coronary disease; and lateral and inferolateral defects were related to left circumflex disease. In each case, the history, age, sex, and characteristic of presenting pain were applied to the determination of coronary disease likelihood by the method of Diamond and Forrester (*28*). The electrocardiogram, stress test, and other clinical studies could potentially be used to determine the prestress imaging coronary disease probability by a Bayes' method approach (*29*) but were not used because of the spectrum of available data among patients studied. Coronary angiography was available in 6 patients within 6 mo of perfusion imaging to confirm the expected location of perfusion defects. The pattern of the emission bull's eye map, scaled to the relative count intensity, was compared in each patient with the relative detection likelihood on the detection bull's eye map. In the emission images, defects with intensity ≥60% of peak activity were mild, 40%–60% of peak were moderate, and <40% were severe. When the regional detection likelihood on the emission bull's eye map was reduced beyond the relative count intensity on the emission bull's eye map, scaled and graded in the same increments, the apparent defect was said to be strongly related to attenuation. When the relative count intensity on the emission bull's eye map was reduced beyond the regional detection likelihood on the emission bull's eye map, the apparent defect was said to be related to regional underperfusion.

RESULTS

Parameter Estimation

The results of our calculations to estimate the needed parameters are summarized. First, whereas the narrow-beam, linear attenuation coefficient for water is approximately $\mu_{high} = 0.14$ 1/cm at 170 keV and $\mu_{low} = 0.19$ 1/cm at 75 keV, our calculations yielded an apparent attenuation coefficient of $\mu_{high} = 0.12$ 1/cm and $\mu_{low} = 0.15$ 1/cm for the object geometry used for these calculations. The calculated apparent attenuation coefficients are consistent with experimental observations reported by others (*30,31*). The ratio of the number of high- and low-energy primary ^{201}Tl emissions was determined to be approximately $N_o^{high}/N_o^{low} = 0.11$, similar to the true ratio of the physical emission rates of $N_o^{high}/N_o^{low} = 0.10$. Therefore, we used the following parameter values for all dual-energy studies reported below: $\mu_{high} = 0.12$ 1/cm, $\mu_{low} = 0.15$ 1/cm, and $N_o^{high}/N_o^{low} = 0.11$.

Phantom Studies

Uniformity Phantom. Detection probability profiles are shown for both the 360° study in Figure 2 and the 180° study in Figure 3. Qualitatively, the agreement between the simulations and the phantom measurements is excellent. The simulations predict a relatively flat detection probability for a 360° acquisition with the 20-cm-diameter phantom. In this case, attenuation tends to favor detection of emission events near the edge of the cylinder versus the center; however, this is offset by the detection of a larger number of scattered photons from the center of the cylinder relative to the edge. For the 180° acquisition, as expected, the simulations predict that the detection probability near the top surface of the cylinder is significantly greater than that near the bottom surface. This reflects the fact that detected γ-rays that were emitted near the top of the cylinder traverse, on average, a much shorter pathlength through water than γ-rays emitted from the lower regions of the cylinder.

Computer Simulation. The polar images of the reconstructed MCAT phantoms are shown in Figure 4A, with the corresponding IDEP polar maps and the calculated detection probability polar maps shown. In the case of the large female model, both the IDEP-estimated detection probability and the calculated detection probability maps show characteristic lower detection probabilities in the inferolateral and inferoseptal portions of the bull's eye images, which correspond to lower reconstructed values in the polar map of the FBP-reconstructed image. The case is very similar for the male model for the inferolateral section of all bull's eye images. The simulated phantoms parallel what we expect clinically in relation to men and women. In both cases, there is evidence of attenuation, giving an inferior defect. However, in women there is greater attenuation from overlying breast, which is generally reflected anteriorly. This is evident

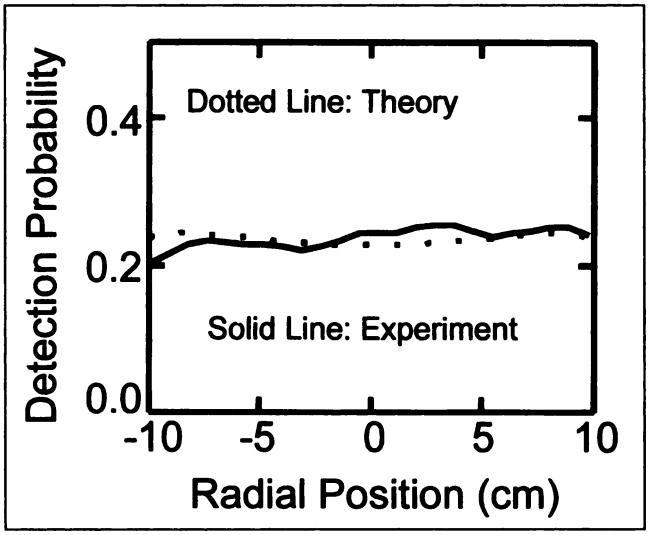

FIGURE 2. Cylindric phantom: 360° acquisition. Shown is comparison of detection probability reconstructed with 360° dual-energy projection data (solid line) versus simulation results (dotted line). Comparison is made along profile through center of 20-cm-diameter cylindric phantom.

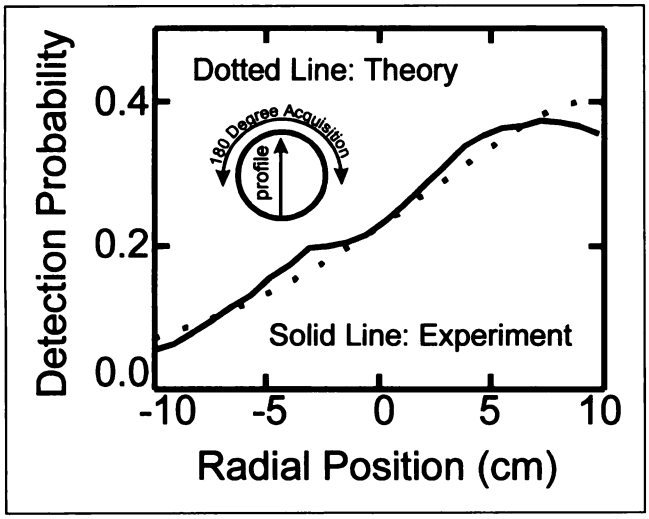

FIGURE 3. Cylindric phantom: 180° acquisition. Shown is comparison of detection probability reconstructed with 180° dual-energy projection data (solid line) with simulation results (dotted line). Comparison is made along central vertical profile through 20-cm-diameter cylinder, with emission projection data acquired over arc shown in inset.

in the phantom study where reduced intensity is evident in the female phantom compared with the male phantom from 9 to 1 o'clock on the polar map clock face, the appropriate location for the presence of anterior attenuating breast tissue. As in patients, changes are seen in this anterior location, whereas inferior and inferolateral distributions remain the same. The greater anterior attenuation in the women makes the polar map somewhat more homogeneous than that of the men, again reflecting the situation observed in patients.

Figure 4B graphs the calculated detection probabilities in the polar map against the IDEP-estimated detection probabilities (from Fig. 4A) for the 2 digital phantoms and shows good correlation (r = 0.93 and 0.96) between the 2 values. Note that the detection probability values are only relative. Clearly, in these noise-free, scatter-free simulations of realistic patient geometries, the IDEP-estimated detection probabilities are well correlated with the actual detection probabilities.

Patient Studies

The tabulation of patient results is shown in Table 2. Six patients, sent primarily for angiography because of the results of imaging, were confirmed to have coronary disease. This was limited to 1 vessel in 2 patients, 2 vessels in 1 patient, and 3 vessels in 3 patients. Five other patients without angiography had a history, an electrocardiogram,

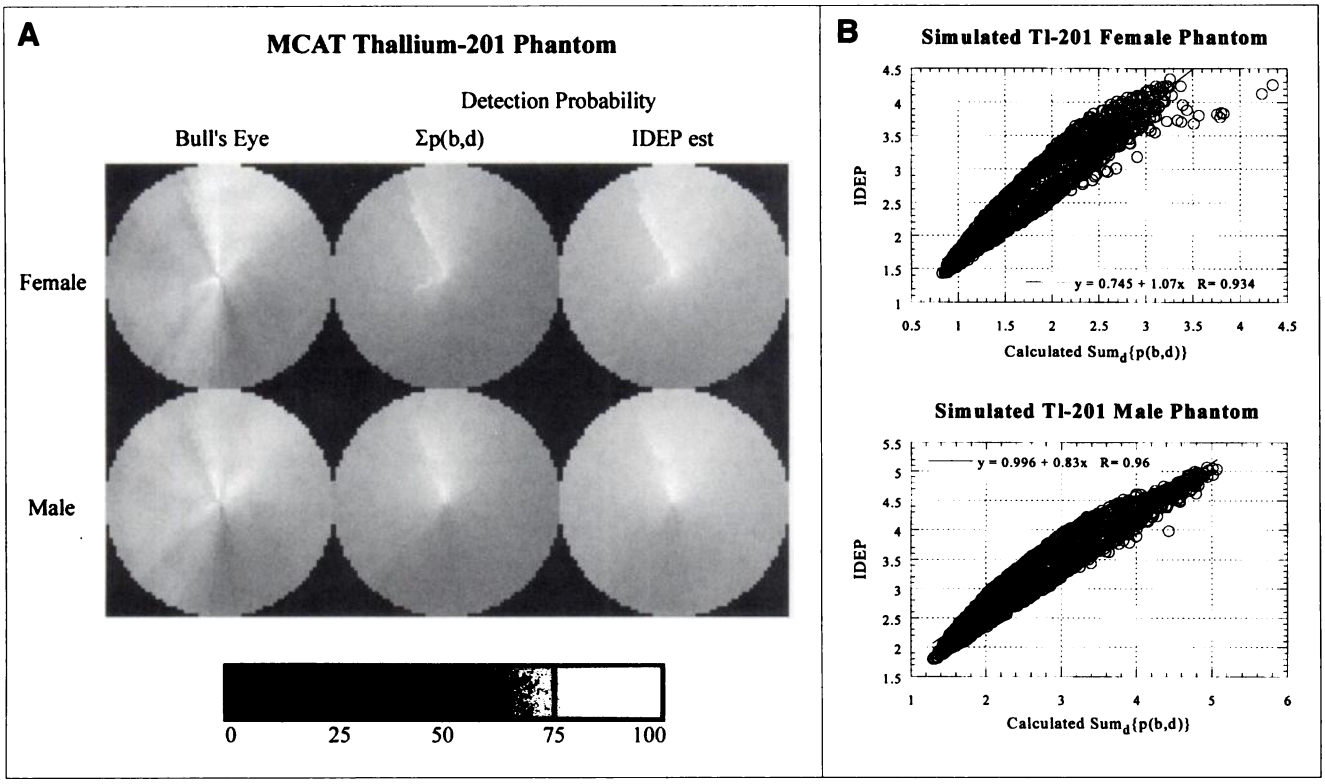

FIGURE 4. Phantom reconstructions of simulated patient studies. (A) Bull's eye maps of distribution of activity, emission map (left), and probability of detection maps derived from 2 ^{201}Tl MCAT phantoms. Probability of detection maps is derived from known phantom attenuation distributions (center) and from IDEP calculations (right). Both agree with each other and reflect probability of photon detection. (B) Comparisons of detection probabilities: plots of calculated versus IDEP-predicted detection probabilities for simulated large woman and large man, whose bull's eye plots are shown above. Individual points on plot are spatially correlated locations on each of bull's eye plots shown above. There was excellent correlation in each model: r = 0.93 and r = 0.96, respectively.

TABLE 2
Study Patients

Patient no.	Age (y)	Sex	Stress	Cardiac diagnosis	LVF	ECG	Sx	CLk	E	IDEP	I
1	65	M	D	HCM	Normal	LVH	ACP	Low	Mild inf and post-sept (RCA)	Mildly reduced inf and post-sept	Normal
2	83	F	D	HTN	Normal	Normal	New ACP	Low	Reduced inf (RCA)	Homogeneous, more inf, less apex	Normal
3*	78	M	D	CAD, prior IMI	Reduced	Q in II, III, AVF	Preop	CAD, 3VD	Sev ant and post-sept, inf and inf-lat, and apex (3VD)	Mild inf and post-sept	3VD
4*	75	M	D	CAD, CABG, PTCA, HTN	Reduced	NS ST-T	ACP	3VD	Sev reduced inf, inf-lat, ant and post-sept, apex, mod ant (3VD)	Mild inf, inf-lat	3VD
5*	72	M	Ex	CAD, CABG	Normal	Normal	Recurrent CP	Patent grafts, advanced native RCA disease	Sev inf and post-sept (RCA)	Mild decreased inf and post-sept	RCA
6*	45	F	D	CAD, prior AMI	Reduced	ST-T (abnormalities)	ACP	LAD	Sev ant, ant-lat, ant-sept, apical with mod inf (LAD, RCA)	Mod inf	LAD
7	48	M	D	DM, COPD	Normal	Normal	ACP	Low	Homogeneous uptake, greatest at apex (normal)	Homogeneous, less at apex	Normal
8*	71	F	D	CAD, prior ASMI	Reduced	Q waves ant	NACP	LAD, RCA	Sev post-sept, inf with mod reduced ant, ant-sept, ant-lat, and inf-lat (3VD)	Mod inf, inf-lat, post-sept	LAD, RCA
9*	70	M	Ex	CAD, prior IMI	Reduced	Q in II, III, AVF	ACP	3VD	Sev ant, ant-sept, post-sept, inf, inf-lat, apical (3VD)	Mild inf	3VD
10	47	M	Ex	chol	Normal	Normal	ACP	Low	Mod inf, post-sept (RCA)	Mod inf, post-sept	Normal
11	58	M	Ex	HTN, chol	Normal	RBBB	ACP	Low	Mod inf, post-sept (RCA)	Mod inf, post-sept	Normal

*Recent coronary angiography.

Stress = nature of stress test; LVF = left ventricular function; ECG = electrocardiogram; Sx = presenting symptoms of test indications; CLk = coronary disease likelihood; E = pattern on emission bull's eye display; IDEP = pattern on IDEP bull's eye display; I = final impression; D = dipyridamole; HCM = hypertrophic cardiomyopathy; LVH = left ventricular hypertrophy; ACP = atypical chest pain; Low = low coronary disease likelihood; inf = inferior; post-sept = posteroseptal; RCA = right coronary artery involvement; HTN = hypertension; CAD = coronary artery disease; IMI = inferior myocardial infarction; AVF = ECG lead AVF; Pre-op = preoperative evaluation; 3VD = 3-vessel coronary disease; sev = severe; ant = anterior; inf-lat = inferolateral; CABG = coronary artery bypass grafting; PTCA = percutaneous transluminal coronary angioplasty; NS = nonspecific; mod = moderate; Ex = exercise; CP = chest pain; AMI = anterior myocardial infarction; ant-lat = anterolateral; ant-sept = anteroseptal; LAD = left anterior descending coronary involvement; DM = diabetes mellitus; COPD = chronic obstructive lung disease; ASMI = anteroseptal myocardial infarction; NACP = nonanginal chest pain; chol = increased cholesterol; RBBB = right bundle branch block.

and clinical studies consistent with a low (<15%) likelihood of coronary artery disease. Qualitative results from 4 of the 11 patients are shown in Figure 5, which presents a series of reoriented cardiac slices along with a quantitative characterization of the emission and detection probability information of stress studies in the form of bull's eye plots scaled to relative emission counts and detection likelihood, respectively. When the relative detection likelihood was applied to modify the apparent emission distribution, regions of decreased emission were found correctly to be related to attenuation in 6 vascular areas, 5 in the right and 1 in the circumflex region, in 6 patients (4 with a low likelihood of coronary disease). Apparent defects were confirmed to be related to perfusion in 13 vascular areas in 7 patients. Although the diagnostic sensitivity was unchanged, coronary disease was excluded in the 4 patients with a low

likelihood of coronary disease, and an uninvolved vascular bed was excluded in a patient with 2-vessel disease.

As is clearly evident from Figure 5, there is a systematic trend, well above the noise, for overall decreasing detection probability when moving from apex to base and from anterolateral wall to inferoseptal wall. This trend is qualitatively present in all 11 patient studies examined to date. In addition, this qualitative trend is consistent with our expectations that attenuation at the apex generally is less severe than that at the base because of the proximity of the apex to the chest wall. A similar argument applies for the anterior wall versus the inferior wall.

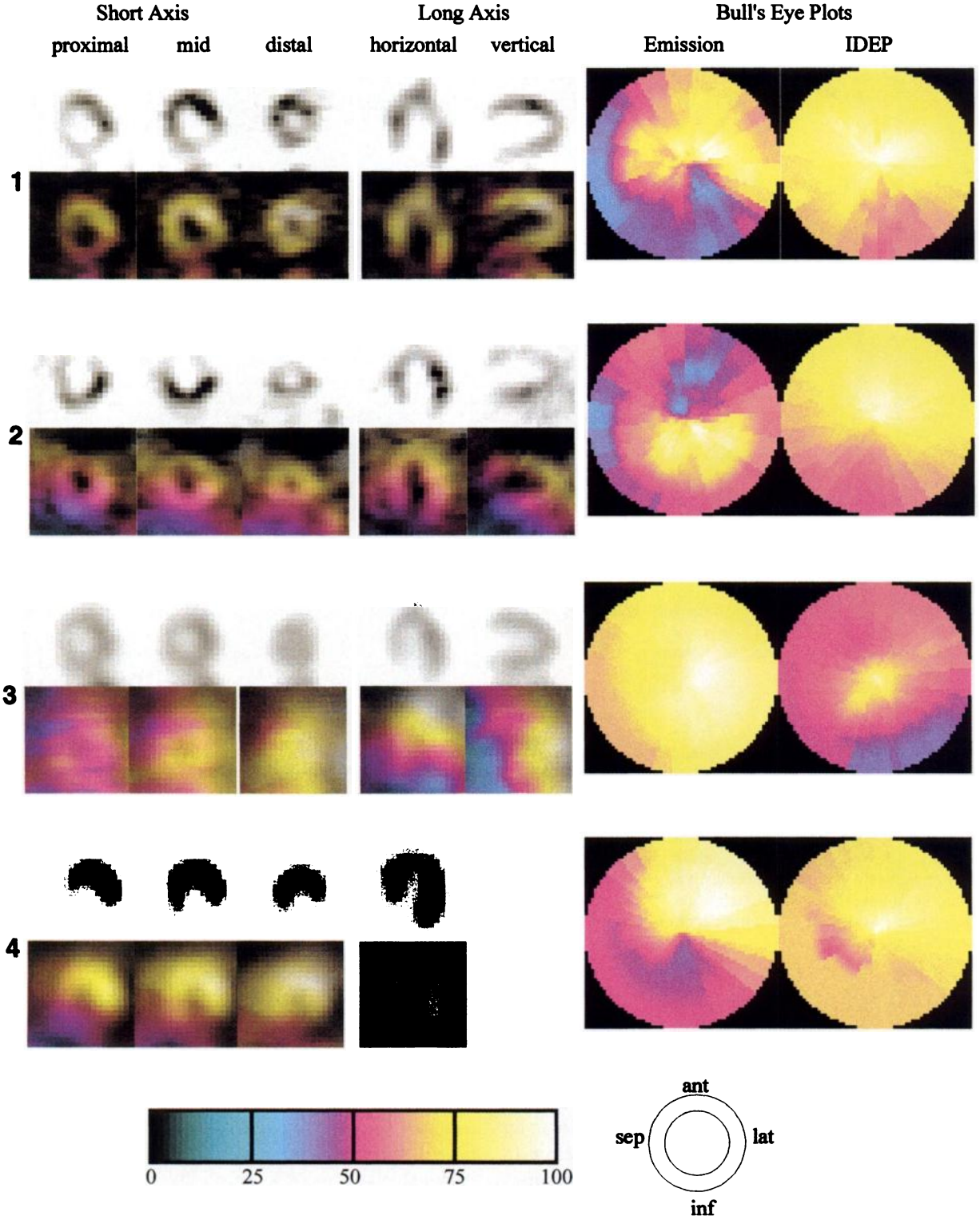

DISCUSSION

Reconstruction of Probability Distribution Maps with IDEP

Although many factors influence the accuracy and precision achievable with IDEP, the most significant limitation in our initial implementation of IDEP is its sensitivity to the limited number of γ-rays detected in a typical SPECT myocardial perfusion study. As observed by Hansen and Siegel (22), the very low emission rate of 167-keV γ-rays from ^{201}Tl impacts dramatically the precision with which attenuation can be characterized using dual-energy window measurements because N_o^{high} is smaller by a factor of ~10 than N_o^{low}. Furthermore, on an absolute basis, in the clinical cases examined thus far it is not uncommon for N^{high} to be <10 counts in some pixels, even when viewing regions of relatively high activity. Thus, estimates of the attenuator geometry using this technique can vary substantially, even if N^{high} changes by 1 count. Another problem related to photon statistics arises when zero counts are detected in 1 of the energy windows. Currently, if either N^{high} or N^{low} is zero, we assume that the attenuating region extends throughout the cross-sectional field of view (i.e., L = S). One consequence of this is that the detection probability may be underestimated along projections that view little or no radionuclide. This is a rationale for developing an analysis method, such as IDEP, that is less sensitive to these projections. This potential underestimate of the detection probability along any 1 view is partially offset by the fact that any 1 location is averaged over many views. Obviously, future work will involve more systematic investigations of these considerations and exploration of other physical effects such as noise and scatter.

The reconstruction of a detection probability map offers certain advantages, particularly in terms of controlling the poor photon statistics and the ill-conditioned nature of reconstructing a patient-specific attenuation map from dual-energy ^{201}Tl projection data. Although the detection probability map and the attenuation map are closely related, they are distinctly different in that the detection probability is related to the attenuation distribution through an integral equation (Eq. 3). In particular, the detection probability at a point within a volume is related to a set of line integrals through the volume that depend on the SPECT acquisition protocol (e.g., a 360° acquisition versus a 180° acquisition). Although reconstruction noise may overwhelm attempts to reconstruct attenuation maps from the emission data, the reconstruction noise in the detection probability map for the same system is reduced significantly because it undergoes an additional averaging process (through the integral relationship). Furthermore, projections through these regions are usually not plagued by zero-count projection measurements. Thus, these methods do not require the generation of attenuation maps and can be calculated in regions containing or surrounded by relatively high radionuclide concentrations without requiring a calculation external to these regions.

Interpretation of IDEP Model

The detection probability image characterizes the magnitude and position of attenuation artifacts in conventionally reconstructed myocardial perfusion images and is supplementary to the SPECT images used conventionally by the reading physician. Therefore, we expect that for physicians, who predominantly interpret conventional perfusion images, the IDEP technique will require reduced physician training or retraining time compared with interpreting attenuation-compensated images. Second, the reconstruction of a detection probability map is less sensitive to poor photon statistics and the ill-conditioned nature of reconstructing a patient-specific attenuation map from dual-energy ^{201}Tl projection data. Finally, detection probabilities can be calculated using transmission images, so some of the methods proposed here can be applied to SPECT systems with transmission capabilities independent of the use of dual-energy imaging. Such detection probability data could be potentially valuable as training tools, especially for physicians more accustomed to interpreting images not corrected for attenuation.

FIGURE 5. Patient studies shown for each of 4 patients are short-axis and long-axis slices, emission (above) and painted with its regional detection probability as derived from IDEP method (below); and emission bull's eye and probability detection (IDEP) bull's eye displays painted in same relative intensity scale. Patient 1: 75-y-old man studied with pharmacologic stress testing 7 y after coronary bypass surgery. Emission data reveal dense anteroseptal and posteroseptal, inferior and inferolateral, and apical defects with modest anterior defect. Detection probability plots reveal only evidence consistent with modest inferior attenuation effect. Angiography revealed severe disease in native left anterior descending and left main coronary arteries and in left anterior descending and right coronary graft. Patient 2: 45-y-old woman with prior anterior infarction and known severe proximal single-vessel left anterior descending coronary disease. Emission data reveal dense anterior, anteroseptal, anterolateral, and inferior abnormalities, which are countered on detection probability plots with evidence consistent with only inferior attenuation, equal in intensity to apparent emission defect. Latter finding suggests that in this woman, anterior, anteroseptal, and anterolateral defects are related to perfusion, whereas inferior defect on emission studies is related to attenuation, which correlates well with known anatomy. Patient 3: large 47-y-old man with nonanginal chest pain, diabetes mellitus, chronic obstructive lung disease, and negative treadmill test to a high double product. Emission slices and bull's eye display are relatively homogeneous with most intense activity in apex. IDEP detection probability map reveals evidence consistent with homogeneous reduced detection, least in apex, which helps to explain intense apex on emission plot. Findings are consistent with normal perfusion in this man with low likelihood of coronary disease. Patient 4: 78-y-old diabetic man with known 3-vessel coronary disease. Emission slices and bull's eye map derived from dipyridamole stress testing reveal relatively dense inferior, inferolateral, posteroseptal and anteroseptal, and apical defects. Detection probability plots are consistent with relatively mild attenuation that would have no influence on perfusion pattern, which is consistent with anatomy. sep = septal; ant = anterior; lat = lateral; inf = inferior.

We wish to reiterate that the detection probability map (no matter how calculated) is related to the attenuation map through an integral equation (Eq. 3). Therefore, pixel-by-pixel division of reconstructed images with the detection probabilities will not correct reconstructed SPECT images for errors associated with attenuation. This is clear if one realizes that the attenuation maps are independent of SPECT acquisition protocol, but the detection probabilities are very dependent on the nature of the protocol. This observation highlights the essential difference between our current objectives and those of other investigators, including Hansen and Siegel (*22*). Our initial goal is to characterize the local impact of attenuation on tomographic images with complementary information, not to correct tomographic images for the effects of attenuation. We have developed a method to do this on the basis of the differences in energy for photons emitted from ^{201}Tl.

The value of the detection probability image has not yet been fully appreciated. It is certain that the detection probability can be calculated directly from a patient-specific attenuation estimate, usually obtained through transmission scanning. The results of our calculations and simulations show that detection probabilities can be estimated using the information available from differential attenuation alone. However, the detection probability couples the effects of attenuation and the acquisition protocol, making the interpretation complex. In addition, the absolute and relative values of the estimated detection probability at specific locations relative to those values reconstructed in the emission image have not yet been established.

We emphasize that the attenuating regions used in this technique represent an artificial construct designed to help motivate and describe IDEP. The calculated positions of the attenuating regions have limited physical meaning within this construct. For example, it should not be expected that the positions of the attenuating regions calculated as part of IDEP should align with an external patient-body contour. Moreover, the configuration of the modeled attenuating region between the point source and the detector does not relate directly to the actual attenuation geometry of the object being imaged. Their positions are much more closely related to the average attenuation coefficient between the edge of the body and the position of significant radionuclide concentration (e.g., myocardium). If the average attenuation in this region for a particular projection is greater than water (our reference material), then the calculated position of the attenuating region will tend to lie outside the patient. For example, this might occur for projections through the sternum. Similarly, if the average attenuation in the aforementioned region for a particular projection is less than water, then the calculated position of the attenuating region will tend to lie within the patient. This might occur in projections that intersect the lung. Thus, the model supports nonuniform attenuation. Specifically, for the example of MPI with ^{201}Tl, IDEP accounts approximately for the nonuniform distribution of attenuators in the thorax. Also, various tissues, such as bone, fat, or lung, can occur within this region and will effectively be modeled as forms of high-density or low-density water.

Although this preliminary report suggests a high sensitivity and specificity of the perfusion evaluation method, the numbers are small and we cannot comment on image accuracy. Whereas image interpretation, primarily its specificity, appears to be enhanced by application of the IDEP method, it should be noted that IDEP was not applied for clinical decision making. Here, the identification of coronary disease based on interpretation of the emission images alone was perfect, and its distribution was nearly so in 11 patients. However, its exclusion was imperfect in this small population on the basis of standard clinical and imaging analytic methods. Prone imaging and other interpretive tools, such as gating, were not applied. At most, the current data suggest that IDEP could add an increased objectivity to the recognition of attenuation effects and may aid in more specific identification of perfusion defects. Similarly, we did not apply the method to the evaluation of defect reversibility or the assessment of regional viability. We simply sought to relate emission and detection probability patterns for the identification of true perfusion-related defects in the stress perfusion image. Although seemingly promising, this method both needs and deserves more study.

CONCLUSION

We have developed an IDEP method that estimates the detection probability of emission data as a means of characterizing the impact of photon attenuation in ^{201}Tl myocardial perfusion tomography. IDEP is a software-only approach for considering attenuation that can be applied on existing SPECT systems without the need to purchase or modify an existing system to add transmission capabilities; there are no concomitant maintenance and training costs. Intrinsic dual-energy imaging provides information about the inhomogeneous nature of a patient's thorax, which complicates attenuation compensation within this region. IDEP is computationally efficient, requiring approximately twice as much computing time as FBP reconstructions in its current implementation. No additional camera time or radiopharmaceuticals are needed, and there is no additional radiation dose to the patient. Our use of detection probabilities, if they prove valuable, extends beyond our uses with intrinsic dual-energy imaging because the detection probabilities can also be calculated using transmission images. Thus, they potentially provide an additional input for objectively (i.e., quantitatively) interpreting myocardial perfusion studies performed with SPECT. Initial patient applications appear promising.

ACKNOWLEDGMENTS

This study was supported by a Clinical Research Grant from ADAC Laboratories (Milpitas, CA). The authors also acknowledge support from National Institutes of Health

grant 2 R02 CA50539. Support was also provided by a Graduate Opportunity Fellowship from the Joint Bioengineering Graduate Group at the Berkeley and San Francisco campuses of the University of California. This research was performed during the tenure of an Established Investigatorship from the American Heart Association.

REFERENCES

1. Patterson R, Horowitz S, Eisner R. Comparison of modalities to diagnose coronary artery disease. *Semin Nucl Med.* 1994;24:286–310.
2. Beller G. Myocardial perfusion imaging with thallium-201. *J Nucl Med.* 1994;35:674–680.
3. Van Train KF, Garcia E, Maddahi J, et al. Multicenter trial validation for quantitative analysis of same-day rest-stress technetium-99m-sestamibi myocardial tomograms. *J Nucl Med.* 1994;35:609–618.
4. DePuey E, Garcia E. Optimal specificity of thallium-201 SPECT through recognition of imaging artifacts. *J Nucl Med.* 1989;30:441–449.
5. Dunn R, Wolff D, Wagner S, Botvinick E. The inconsistent pattern of thallium defects: a clue to the false-positive perfusion scintigram. *Am J Cardiol.* 1981;48:224–232.
6. Tamaki N, Yonekura Y, Kadota K, Kambara H, Torizuka K. Appearance of breast attenuation artifacts with thallium myocardial SPECT imaging. *Clin Nucl Med.* 1985;10:694–696.
7. Eisner R, Tamas M, Clononger K, et al. Normal SPECT thallium-201 bull's-eye display: gender differences. *J Nucl Med.* 1988;29:1901–1909.
8. Frey E, Tsui B, Perry J. Simultaneous acquisition of emission transmission data for improved Tl-201 cardiac SPECT imaging using a Tc-99m transmission source. *J Nucl Med.* 1992;33:2238–2245.
9. Tung C-H, Gullberg G, Zeng G, Christian P, Datz F, Morgan H. Non-uniform attenuation correction using simultaneous transmission emission converging tomography. *IEEE Trans Nucl Sci.* 1992;39:1134–1143.
10. Jaszczak R, Gilland D, Hanson M, Jang S, Greer K, Coleman R. Fast transmission CT for determining attenuation maps using collimated line source, rotatable air-copper-lead attenuators and fan-beam collimators. *J Nucl Med.* 1993;34:1577–1586.
11. Tan P, Bailey D, Meikle S, Eberl S, Fulton R, Hutton B. A scanning line source for simultaneous emission transmission measurements in SPECT. *J Nucl Med.* 1993;34:1752–1760.
12. Rockmore AJ, Macovski A. Maximum likelihood estimation for emission tomography. *IEEE Trans Nucl Sci.* 1976;23:1428–1432.
13. Shepp LA, Vardi Y. Maximum likelihood reconstruction for emission tomography. *IEEE Trans Med Imaging.* 1982;1:113–122.
14. Lange K, Carson R. EM reconstruction algorithms for emission transmission tomography. *J Comput Assist Tomogr.* 1984;8:306–316.
15. Tsui B, Zhao X, Frey E, Gullberg G. Comparison between ML-EM WLS-CG algorithms for SPECT image reconstruction. *IEEE Trans Nucl Sci.* 1991;38:1766–1772.
16. Chang LT. A method for attenuation correction in radionuclide computed tomography. *IEEE Trans Nucl Sci.* 1978;25:638–643.
17. Galt J, Cullom S, Garcia E. SPECT quantitation: a simplified method of attenuation scatter correction for cardiac imaging. *J Nucl Med.* 1992;33:2232–2237.
18. Gullberg G, Malko J, Eisner R. Boundary determination methods of attenuation correction in SPECT. In: Esser PD, ed. *Emission Computed Tomography: Current Trends.* New York, NY: Society of Nuclear Medicine; 1983:33–53.
19. Hosoba M, Wani H, Toyama H, Murata H, Tanaka E. Automated body contour detection in SPECT: effects on quantitative studies. *J Nucl Med.* 1986;27:1184–1191.
20. Younes R, Mas M, Bidet R. A fully automated contour detection algorithm: the preliminary step for scatter attenuation compensation in SPECT. *Eur J Nucl Med.* 1988;14:586–589.
21. Segall G, Davis M. Prone versus supine thallium myocardial SPECT: a method to decrease artifactual inferior wall defects. *J Nucl Med.* 1989;30:548–555.
22. Hansen C, Siegel J. Attenuation correction of thallium SPECT using differential attenuation of thallium photons. *J Nucl Med.* 1992;33:1574–1577.
23. Madsen M, Kirchner P, Edlin J, Nathan M, Kahn D. An emission-based technique for obtaining attenuation correction data for myocardial SPECT studies. *Nuc Med Commun.* 1993;14:689–695.
24. Goris M. Of theoretical derivations and empirical evidence [editorial]. *J Nucl Med.* 1992;33:1578.
25. Gullberg GT, Huesman RH, Malko JA, Pelc NJ, Budinger TF. An attenuated projector-backprojector for iterative SPECT reconstruction. *Phys Med Biol.* 1985;30:799–816.
26. Nelson WR, Hirayama H, Rogers DWO. The EGS4 code system. Stanford, CA: Stanford Linear Accelerator Center; 1985.
27. Tsui BMW, Zhao XD, Gregoriou GK, et al. Quantitative cardiac SPECT reconstruction with reduced image degradation due to patient anatomy. *IEEE Trans Nucl Sci.* 1994;41:2838–2848.
28. Diamond GA, Forrester JS. Analysis of probability as an aid to the clinical diagnosis of coronary artery disease. *N Engl J Med.* 1979;300:1350–1358.
29. Patterson RE, Eng C, Horowitz SF. Practical diagnosis of coronary artery disease: a Bayes' theorem nomogram to correlate clinical data with noninvasive exercise tests. *Am J Cardiol.* 1984;53:252–256.
30. Leichter I, Weinreb A, Hazan G. The effective attenuation coefficient of soft tissue in the presence of Compton scattering from bone: experiments on models. *Phys Med Biol.* 1980;25:711–717.
31. Harris C, Greer K, Jaszczak R, Floyd C, Fearnow E, Coleman R. Tc-99m attenuation coefficients in water-filled phantoms determined with gamma cameras. *Med Phys.* 1984;11:681–685.